

Self-Parameterization Based Multi-Resolution Mesh Convolution Networks

Shi Hezi, Jiang Luo, Zheng Jianmin

HP-NTU Digital Manufacturing Corporate Laboratory, Nanyang Technological University

Zeng Jun

HP Labs

Abstract

This paper addresses the challenges of designing mesh convolution neural networks for 3D mesh dense prediction. While deep learning has achieved remarkable success in image dense prediction tasks, directly applying or extending these methods to irregular graph data, such as 3D surface meshes, is nontrivial due to the non-uniform element distribution and irregular connectivity in surface meshes which make it difficult to adapt downsampling, upsampling, and convolution operations. In addition, commonly used multiresolution networks require repeated high-to-low and then low-to-high processes to boost the performance of recovering rich, high-resolution representations. To address these challenges, this paper proposes a self-parameterization-based multi-resolution convolution network that extends existing image dense prediction architectures to 3D meshes. The novelty of our approach lies in two key aspects. First, we construct a multi-resolution mesh pyramid directly from the high-resolution input data and propose area-aware mesh downsampling/upsampling operations that use sequential bijective inter-surface mappings between different mesh resolutions. The inter-surface mapping redefines the mesh, rather than reshaping it, which thus avoids introducing unnecessary errors. Second, we maintain the high-resolution representation in the multi-resolution convolution network, enabling multi-scale fusions to exchange information across parallel multi-resolution subnetworks, rather than through connections of high-to-low resolution subnetworks in series. These features differentiate our approach from most existing mesh convolution networks and enable more accurate mesh dense predictions, which is confirmed in experiments.

1. Introduction

This paper considers 3D mesh dense prediction tasks such as instance segmentation, semantic segmentation, monocular depth estimation, human pose estimation, and shape correspondence, which are often required in geometric modeling and analysis. In the past decade, deep learning has achieved remarkable success in various 2D/3D applications, including dense predictions in computer graphics and vision. Some well-known networks such as AlexNet [1], VGG [2] and ResNet [3] have been developed. However, dense predictions are position-sensitive and often require element-level predictions, making classical network architectures that first encode the input data into low-resolution representations unsuitable for these tasks. Therefore, new architectures and strategies are needed to achieve accurate dense predictions.

There are typically three approaches to generating high-resolution representations for images using convolutional neural networks (CNN). The first approach involves a high-to-low and low-to-high process, which recovers high-resolution features through upsampling operations [4, 5] and skip-connections [6, 7]. The second approach is to build an image pyramid with pyramid pooling modules [8] or atrous spatial pyramid pooling [9, 10]. The pyramid features are then fused to generate high-resolution representations. The third approach maintains high-resolution channels through the high-to-low and low-to-high process, together with repeated multi-scale feature fusion modules, which produces representations with rich semantic meaning [11, 12]

and has been reported to achieve state-of-the-art dense prediction performance.

Applying and extending CNN frameworks for 3D mesh dense prediction is a tempting idea, but the irregular structure of 3D meshes presents a challenge. Basic CNN operators, such as convolution, pooling, and unpooling, need to be specifically designed to work with non-grid structures. Recently, some approaches have been proposed to mimic CNN networks, such as MeshCNN [13] and PDMeshNet [14], which utilize sequential edge collapses to produce a lower-resolution mesh. However, the selection of edges for collapse depends on specific learning tasks, and training samples may have specific regions that never collapse. This may raise the requirement for diversity of training data and increase the complexity of training networks. Another approach, SubdivNet [15], proposes to remesh the irregular input mesh into a semi-regular structure with subdivision sequence connectivity. However, this approach applies the network operators to the remeshed model instead of the original mesh, making the method dependent on the remeshing results.

Thus one question arises: *can we construct a neural network defined directly on irregular mesh data whose local receptive fields can grow uniformly after each convolution, pooling, or unpooling layer?* Though the terms “irregularity” and “uniformity” seem contradictory, this paper provides a positive answer to this question. In particular, to achieve top-down and bottom-up propagation, we first create a multi-resolution mesh using mesh simplification [16]. To address the challenge of performing basic network operations on the irregular connectivity of a triangular mesh, we construct bijective piecewise linear surface-to-surface maps between meshes of adjacent levels, inspired by inter-surface mapping [17]. Specifically, we map each triangle of a coarse mesh to a “curved” triangle on the fine mesh. The curved

*Corresponding author

Email address: luo.jiang@ntu.edu.sg (Jiang Luo)

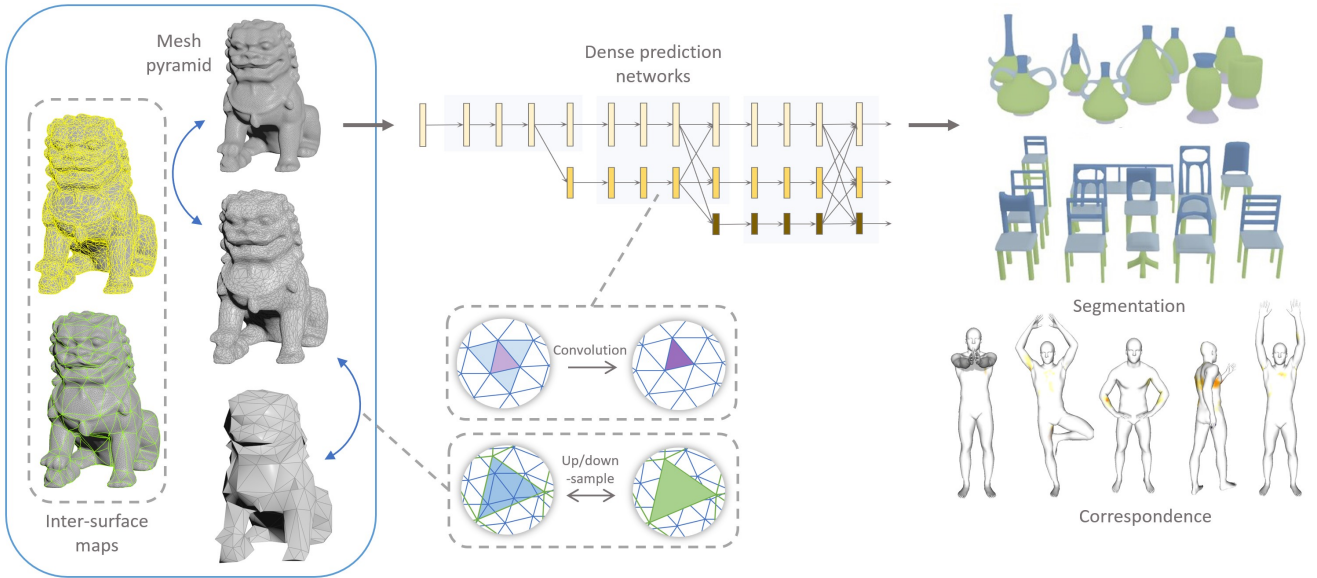


Figure 1: We construct a multi-resolution mesh pyramid from high-resolution input meshes using bijective surface-to-surface maps for any pair of adjacent meshes in the pyramid (left). Based on this, we design down-/up-sampling operators that enable us to easily adapt classic CNN dense prediction architectures and we construct a multi-resolution convolution network that maintains high-resolution representations throughout the network (middle). The resulting networks allow for both high-to-low and low-to-high feature aggregations, leading to high performance in mesh dense predictions (right).

triangle consists of polygonal pieces on the fine mesh, which we can use to design area-aware pooling/unpooling and face convolution layers. For example, in the pooling layer, we merge all the polygonal pieces associated with a curved triangle into one, and the contribution of each polygonal piece is proportional to its area. The key to our approach is that the inter-surface mapping *redefines* the input mesh rather than *reshaping* it. This provides guidance for feature propagation without introducing approximation errors or worrying about the irregularity of the input data. Furthermore, we control the triangle quality during the construction of the multi-resolution mesh, as described in [16, 18], to ensure that the triangles in each level have similar shapes. Additionally, we can constrain the surface-to-surface maps to minimize significant distortion. As a result, the local receptive fields of our network have a relatively fixed pattern and expand uniformly during the layer-by-layer pass, similar to powerful 2D CNNs. Finally, we propose to maintain the high-resolution representation in the multi-resolution convolution network, which enables multi-scale fusion to exchange information across parallel multi-resolution subnetworks and avoids loss of information in the high-to-low process. The overview of our approach is illustrated in Figure. 1.

The contributions of the paper are three-folds. First, we propose a new method for constructing a multi-resolution mesh pyramid associated with piecewise bijective surface mapping among adjacent levels of the mesh. Second, we design novel area-aware pooling/unpooling and face convolution operations that leverage the bijective surface-to-surface mapping to achieve efficient mesh feature learning. Third, by utilizing our multi-resolution architectures and novel operators, we introduce a new framework called *Self-Parameterization Based Multi-Resolution Mesh Convolution Networks* (SPMM-Net), built on existing CNN architecture HRNet [11, 12], to tackle mesh dense prediction tasks. The experiments demonstrate that our proposed method achieves better performance than the state-of-the-art.

2. Related Work

This section briefly reviews some related work, which includes geometric deep learning, especially those adapting classic image dense prediction architectures to mesh structures, and inter-surface mapping.

2.1. Geometric Deep Learning for 3D Shape

A surface mesh is composed of vertices, edges, and faces. Geometric deep learning methods perform convolution in local Euclidean neighborhoods based on the connectivity of vertices or the topology of surfaces. Various convolution operations have been designed. The methods that perform convolution on vertices consider the spatial relations of vertices using Cartesian, polar or spherical coordinates, and define weights between vertices accordingly. Early approaches focused on adapting grid CNNs to irregular graph data. GCNN [19] proposed building a local geodesic system in polar coordinates for each node and discretizing neighboring nodes into a fixed number of bins to handle nodes without a fixed number of neighbors. MoNet [20] represented the learnable convolution kernel in 3D space using a Gaussian Mixture Model (GMM), while SplineCNN [21] extended MoNet with a more flexible convolution kernel that uses B-spline basis functions in a geometric space, providing more learnable parameters compared to previous methods.

Face-based methods incorporate topological features into mesh faces and use an aggregation mechanism to combine neighboring face features. MeshNet [22] introduced a face rotation convolution block that applies the convolution kernel to three pairs of corner vectors, combining the results with MLP layers to ensure invariance to the order of corner vectors. Another method [23] defines two types of convolutions based on geodesic and Euclidean distances to improve the convolution results. SubdivNet [15] remeshes the input mesh into Loop subdivision connectivity to enable four adjacent faces to be pooled into one face. It also introduces an order-invariant face convolution

and a mesh pooling operation. Instead of using the geometric descriptor, Laplacian Mesh Transformer [24] uses Laplacian spectral decomposition to describe the connectivity of triangles, and employs dual attention mechanism to define the message propagation process.

In edge-based convolution, MeshCNN [13] defines convolution operators directly on edges, leveraging the consistent neighboring structure of edges in a triangular mesh. MeshWalker [25] extracts shape features by walking randomly along mesh edges to sample subgraphs for learning. PD-MeshNet [14] constructs both a primal and a dual graph, enabling the assignment of features to edges and faces as well.

For dense prediction tasks on meshes, adapting existing 2D CNN techniques, such as high-resolution representation recovery and multi-resolution fusion, is an appealing idea. However, defining multi-scale representations on meshes is non-trivial due to their irregular and non-uniform characteristics. Clustering methods, such as Graclus pooling [26] (also called greedy node clustering) and diff-pool [27], have been proposed for graph pooling. Although these techniques work well for some undirected graphs, they may not preserve the manifold structure, resulting in undesirable outcomes. One possible solution is to redesign the pooling operation, for instance, using dynamic edge collapse operations which generate a coarse surface, as demonstrated in MeshCNN [13] and PD-MeshNet [14]. These methods record the indices and positions of the collapsed edges, which can be used to perform upsampling via vertex split operations and thus to adapt CNN dense prediction networks such as U-Net. However, they may result in non-uniform downsampling of edges. Another solution is to build multi-resolution mesh pyramids through remeshing, as shown in SubdivNet [15] and Neural Subdivision [28]. These methods first decimate the input mesh to a base mesh and then construct a semi-regular connectivity by subdividing the base mesh. The semi-regular structure allows for the natural extension of operators in CNN. However, these methods heavily rely on the quality of the remeshing results.

2.2. Inter-surface Mapping

Inter-surface mapping is to create a continuous and bijective surface-to-surface map between two triangle meshes with the same topology. Existing methods can be roughly divided into two categories according to whether they need some intermediate domains or not. The first category employs a unit disk or sphere as the intermediate domain, with each triangular mesh parameterized on this domain. The inter-surface map is then defined as the composite of separate parameterizations [29, 30]. As these methods cannot be directly applied to surfaces with different topologies, cut/transition processes are required [31, 32], which adds extra steps. Recently, constant-curvature metrics have been employed to optimize the end-to-end map without cuts, providing a solution for surfaces with arbitrary genus [33]. The second category uses local optimization to generate a continuous map between discrete surfaces with arbitrary topology [17, 34, 35]. However, this approach is difficult to generate globally optimal maps and also requires either solving a complicated optimization problem or introducing additional processing such as designing cuts, making it time-consuming and difficult to handle large-scale and multi-class datasets.

3. Mesh Pyramid

In our proposed framework, the input mesh must undergo a process to create a mesh pyramid consisting of multiple resolutions from fine to coarse, and a set of bijective surface-to-surface

maps before it is fed into the network. This section presents an enhanced self-parameterization based approach for generating a mesh pyramid and bijective maps between the adjacent levels of the multi-resolution meshes.

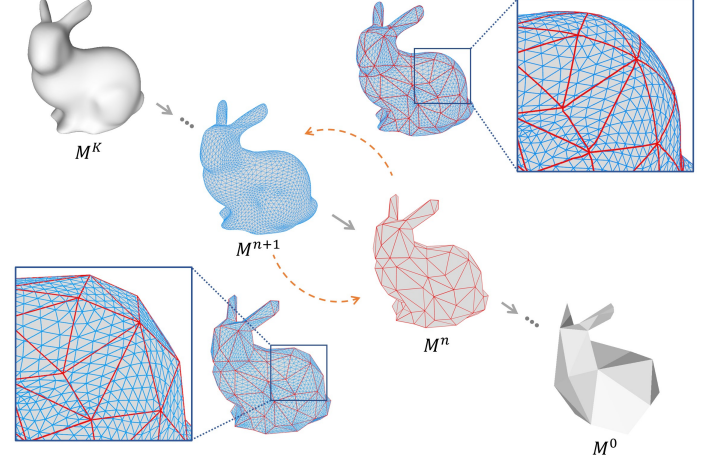


Figure 2: Generating the multi-resolution mesh pyramid from an input mesh. Bijective inter-surface maps between M^{n+1} (blue) and M^n (red) are visualized.

3.1. Notation

The input triangle mesh is 2-manifold and watertight. We denote it by $M = (V, E, F)$, where $V = \{v_i \mid v_i \in \mathbb{R}^3\}$, $E = \{e_i \mid e_i = (v_{i_1}, v_{i_2})\}$ and $F = \{f_i \mid f_i = (e_{i_1}, e_{i_2}, e_{i_3})\}$ are a set of vertices, a set of edges and a set of triangular faces, respectively. Each edge is bounded by two vertices, and each face is bounded by three edges. Two faces are adjacent if they share an edge, and each face f_i has three adjacent faces $\{f_{i_j} \mid j = 1, 2, 3\}$.

With an input mesh M , we define a sequence of decimated meshes (M^K, \dots, M^0) such that $M^K = M$, and M^0 is the base mesh. $K + 1$ is the height of the mesh pyramid we want to create. Moreover, a bijective surface-to-surface map \mathcal{H}^n from M^{n+1} to M^n is also defined, for all $n \in \{K - 1, K - 2, \dots, 0\}$. It is worth pointing out that our $\mathcal{H}^n(\cdot)$ is defined for every point on the mesh M^{n+1} , not just its vertices.

In addition, a sparse matrix $A^n = [a_{i,j}^n] \in \mathbb{R}^{|F^{n+1}| \times |F^n|}$ is computed using the bijective inter-surface map $\mathcal{H}^n : M^{n+1} \rightarrow M^n$, $0 \leq n \leq K - 1$, where $a_{i,j}^n \in [0, 1]$ measures the overlap ratio between face f_j^n of mesh M^n and image $\mathcal{H}^n(f_i^{n+1})$ of face f_i^{n+1} of mesh M^{n+1} . The sparse matrices are used to define the downsampling and upsampling operations between two adjacent pyramid levels.

3.2. Multi-Resolution Mesh Generation

Given a high-resolution input mesh M , our target is to construct a set of multi-resolution meshes $\{M^n\}_{n=0}^K$ and a set of bijective inter-surface maps $\{\mathcal{H}_n : M^{n+1} \rightarrow M^n\}_{n=0}^{K-1}$ (see Figure. 2) such that the triangles of each mesh except M^K (the input one) have a similar shape and all the surface maps have small distortions. Note that such requirements imposed on the triangles and the maps can make our network defined on irregular data more similar to traditional CNN.

Here we present a simple and efficient approach that is based on MAPS [37]. The mesh pyramid can be generated through various implementations, which can either rely on vertex removal

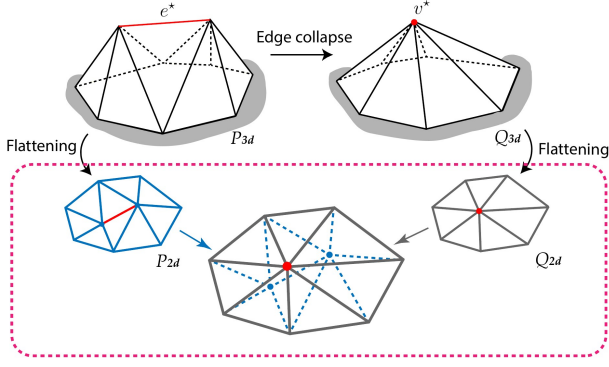


Figure 3: We flatten the one-ring face-neighborhood of e^* using LSCM parameterization [36]. After v^* is generated by QEM in 3D space, we also flatten its one-ring face-neighborhood into the same UV domain.

or edge collapse. We opt for an implementation [28] that utilizes QEM [16] to steer edge collapse in a more balanced way, while disregarding collapses that could result in triangle flips. This helps prevent the production of overly thin or excessively large triangles. Specifically, we repeat the following steps to obtain the subsequent level and corresponding map, using the current mesh.

- (1) Pick an edge e^* of the current mesh to collapse and generate a new vertex v^* . The approach is similar to the QEM method, but it differs in that it uses not only approximation error E_{approx} but also a distortion error to determine the priority of the edge. The distortion error refers to the symmetric Dirichlet energy [17] $E_{distort}$ of the map between two surface patches P_{3d} and Q_{3d} , where P_{3d} and Q_{3d} contain the one-ring neighbourhood of e^* and v^* , respectively, as shown in Figure. 3. We use a weight w to compute a linear combination of two errors: $E = (1-w)*E_{approx} + w*E_{distort}$. To construct such a map, we first flatten P_{3d} and Q_{3d} onto the same UV domain, and then overlay the two parameterizations P_{2d} and Q_{2d} to compute a mutual tessellation. Refer to [30] for more details on constructing a map between two disk-topology meshes and measuring the distortion of that map.
- (2) Now, each vertex v of M^{n+1} contained in P_{3d} is mapped to a triangle of Q_{2d} . We use the point location algorithm [38] to find the index $I(v)$ of the triangle and compute the corresponding barycentric coordinates (α, β) . We compute v 's image $\phi(v)$ in Q_{2d} as follows:

$$\phi(v) = \alpha u_1 + \beta u_2 + (1 - \alpha - \beta) u_3, \quad (1)$$

where u_1, u_2, u_3 are vertex locations of the $I(v)$ -th triangle of Q_{2d} . We define a triplet $\gamma(v) = (I(v), \alpha, \beta)$ to encode $\phi(v)$, as shown in Figure. 4(b).

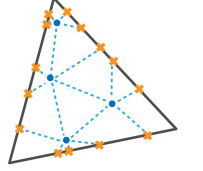
- (3) Each edge e of M^{n+1} contained in P_{3d} is fully or partially mapped to a line segment $\psi(e)$ (see Figure. 4(b)) in Q_{2d} . For each $\psi(e)$, we find all the edges of Q_{2d} that intersect it. Assuming that $\psi(e)$ going from vertex $\phi(v_1)$ to vertex $\phi(v_2)$ intersects an edge of Q_{2d} going from vertex u_1 to vertex u_2 , we solve the following 2×2 linear system to get the intersection point:

$$\lambda_1 \phi(v_1) + (1 - \lambda_1) \phi(v_2) = \lambda_2 u_1 + (1 - \lambda_2) u_2, \quad (2)$$

where λ_1, λ_2 are the linear combination coefficients. All the edge intersection tests can be parallelized.

- (4) For each edge-to-edge intersection point s , we create a quadruplet that stores two indices of incident edges and two linear combination coefficients denoted by $\tau(s) = (J_1, J_2, \lambda_1, \lambda_2)$, where λ_1 is associated with the J_1 -th edge of M^{n+1} , and λ_2 is associated with the J_2 -th edge of Q_{2d} . Now we use a list of quadruplets $\{\tau(s_1), \dots, \tau(s_n)\}$ to encode $\psi(e)$, where $\{s_i\}_{i=1}^n$ are the computed intersection points and are recorded in one halfedge directed from $\phi(v_1)$ to $\phi(v_2)$. Since some of these intersection points may appear on the boundary of Q_{2d} in the following iterations, we record all the quadruplet data in each iteration to judge which edges of M^{n+1} are partially mapped to Q_{2d} in the following iterations, see Figure. 4(b),(c) and (d).
- (5) Update the current mesh locally, replacing P_{3d} with Q_{3d} . Meanwhile, we use recorded codes $(\{\gamma\})$ and $(\{\tau\})$ to relocate the vertices of M^{n+1} on the newly updated mesh and identify the edge-to-edge intersection points on that mesh as well.

After the user-specified number of iterations is reached, we arrive at the n -th level. At this point, we obtain a meta mesh $M^{n+1,n}$ formed by embedding M^{n+1} on M^n , which consists of the embedded vertices of M^{n+1} , the vertices of M^n , and the edge-to-edge intersection points. However, we do not yet know the connectivity of $M^{n+1,n}$. To complete $M^{n+1,n}$, we need to extract the overlay polygon between any pair of intersected triangles. Specifically, for each face of M^n , we use the recorded codes $(\{\gamma\})$ and $(\{\tau\})$ to find all the triangles of M^{n+1} that intersect it, and compute the triangle-to-triangle intersection. For more details of the intersection implementation, refer to [39]. Moreover, in the step (2) and step (4) of the method described above, we can record additional triplets and quadruplets for embedding M^n on M^{n+1} . Thus, we obtain another meta mesh $M^{n,n+1}$ formed by embedding M^n on M^{n+1} (see Figure. 2). Since $M^{n+1,n}$ and $M^{n,n+1}$ have the same connectivity, and each of their faces is a planar convex polygon, the bijective mapping \mathcal{H}^n can be naturally defined in a piecewise linear manner.



Complexity. The QEM [16] algorithm takes $O(\log N)$ time to collapse one edge by removing the least cost from a heap where N is the number of edges; the conformal flattening is a constant cost on top of each edge collapse since valence is bounded, and the edge-to-edge intersections can be implemented in a linear complexity [39] on top of each conformal flattening. Thus, one edge collapse actually takes $O(N)$ time, and the complexity of the entire algorithm is $O(N^2)$. It is worth pointing out that edge-to-edge intersections can be trivially parallelizable, so our algorithm has the potential to be implemented in the complexity of $O(N \log N)$.

4. SPMM-Net

We are now ready to present our network. It takes high-resolution mesh data as input and aims to learn high-level representations for each face, which can benefit downstream dense prediction tasks. Specially, we utilize the mesh pyramid with bijective surface-to-surface maps to design both high-to-low and low-to-high face feature aggregation schemes that provide similar functionality to pooling and unpooling operations in 2D CNNs. Moreover, we define an order-invariant face-based convolution aggregating neighbor information through layers. With flexible downsampling, upsampling, and convolution operations,

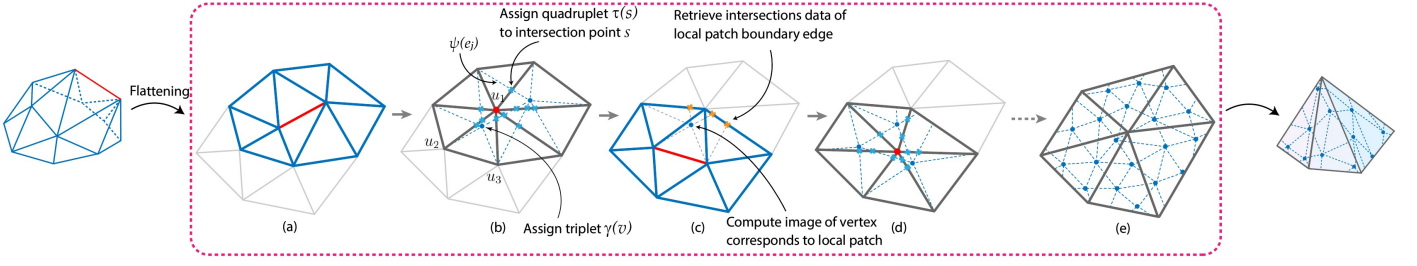


Figure 4: The process of recording and retrieving edge-to-edge intersection information during two consecutive iterations. From left to right: (a) A 3D patch is flattened and the edge e^* is to be collapsed. (b) The intersection points are computed in the UV domain and recorded as quadruplets, while the collapsed vertices are recorded as triplets. (c) In the second iteration, intersection points on the boundary edges of the blue patch are retrieved according to recorded quadruplets, and the triplets corresponding to the blue patch are also updated. (d) Intersection points for inner edges of the local patch are updated. (e) After several iterations, each face of the local patch contains a partial map of M^{n+1} .

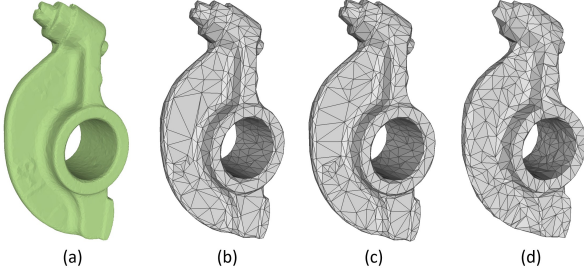


Figure 5: For input mesh (a), we visualize the decimated mesh with different values of weight w for combining the approximation error and the distortion error. $w = 0$ gives the pure QEM simplification that generates shape-preserving decimated mesh (b), while $w = 0.1$ helps the reduction of thin triangles in the decimated result (c), and $w = 0.3$ leads to the result with more uniform-areas (d).

we adapt powerful CNN dense prediction architectures [11, 12] to irregular 3D surface meshes, thus enabling dense prediction tasks on meshes using SPMM-Net (see Figure. 6). The main technical components of our network are detailed in the following subsections.

4.1. Input features

Given an input mesh M , we first embed the shape and location information for each face in F as the input feature. The input feature to the network for each triangular face is a 10-dimensional vector derived from geometry. It consists of a 7-dimensional global feature that describes the triangular face center $\{C_x, C_y, C_z\}$, face area $\{a\}$, face normal $\{N_x, N_y, N_z\}$, and a 3-dimensional vector $\{k_0, k_1, k_2\}$ that describes the relations between each face and its three neighboring faces, which is calculated as the dot product between vertex normals and the face normal [40]. As three vertices of the face are unordered, we remove the ambiguity of the curvature vector by applying the invariant computation:

$$\begin{cases} g_0 = k_0 + k_1 + k_2, \\ g_1 = |k_0 - k_1| + |k_1 - k_2| + |k_2 - k_0|, \\ g_2 = |k_0 - 2k_1 + k_2| + |k_1 - 2k_2 + k_0| + |k_2 - 2k_0 + k_1| \end{cases}$$

The input 10-dimensional vector h_i^F that describes the shape and position of the i -th face is defined as follows:

$$h_i^F = [C_x, C_y, C_z, a, N_x, N_y, N_z, g_0, g_1, g_2]. \quad (3)$$

For convenience, we ignore the use of the index i on the right side of the above equation.

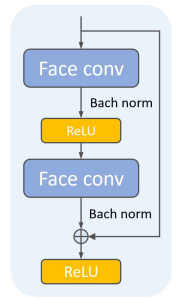
4.2. Parallel convolution block

Convolution operation. In a watertight triangle mesh without boundary edges, each face is adjacent to 3 neighbor faces. Motivated by the convolution operation defined in CNN, which takes a fixed number of 9-pixel representations for each calculation, the basic convolution pattern on a triangular mesh for face f_i is formed by aggregating the features of its 1-ring face-neighborhood $\mathcal{N}(f_i)$. Unlike images, the neighboring face set $\mathcal{N}(f_i)$ in the mesh is unordered, yet the order variance could cause ambiguity in the calculation. In our network, we follow the setting from SubdivNet [15] that utilizes summation to achieve invariance and define the convolution operation on face f_i as follows:

$$h_i^F = w_0 h_i^F + w_1 \sum_{j=1}^3 h_{i_j}^F + w_2 \sum_{j=1}^3 |h_{i_{j+1}}^F - h_{i_j}^F| + w_3 \sum_{j=1}^3 |h_i^F - h_{i_j}^F|, \quad (4)$$

where $\{h_{i_j}^F\}_{j=1}^4$ are the face features of $\mathcal{N}(f_i)$ in counter-clockwise order, $h_{i_4}^F = h_i^F$, and $\{w_i | w_i \in \mathbb{R}^{L \times D}, i = 0, 1, 2, 3\}$ are trainable parameters with L and D being input and output channels, respectively.

In the proposed network, the face features are propagated independently along each resolution level through parallel convolution blocks (see light blue blocks in Figure. 6). Within each parallel convolution block, regular convolutions with identical residual learning strategy [3] are performed over each level. Each convolution block is defined to consist of four residual units, and a residual unit contains two face convolution layers, two batch normalization layers, and two ReLU layers.



4.3. Multi-resolution fusion block

Multi-resolution fusion exchanges information between different resolution levels, which is frequently used in learning architectures for 2D dense prediction. The low-resolution features are likely to contain global semantic information, and high-resolution features are sensitive to local geometry and precise spatial positions. By combining these information, the fused features would be semantically richer and spatially more precise, which thus benefits the downstream tasks.

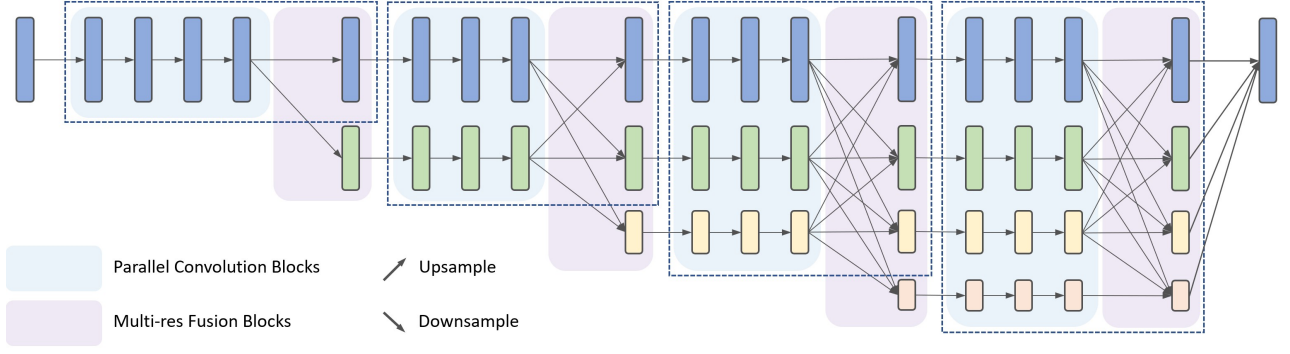
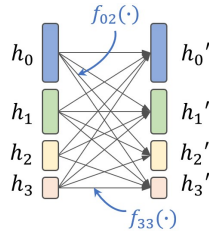


Figure 6: The architecture of SPMM-Net is based on HRNet [12]. The network maintains the input high-resolution mesh across its stages to obtain spatially precise dense prediction results. The network consists of 4 stages (indicated by the dashed line boxes), each of which comprises multiple parallel convolution blocks and multi-resolution fusion blocks. In the parallel convolution block, features are propagated independently along each resolution level. In the multi-resolution fusion block, the high-resolution data are downsampled, and the low-resolution data are upsampled. The different resolution representations are fused by summation to enable information exchange between different resolution levels.

In SPMM-Net, the multi-resolution feature fusion (see lilac blocks in Figure. 6) is performed after each multi-resolution convolution block. The figure on the right illustrates a four-level fusion block, where the input features to the fusion block are: $\{h_r\}_{r=0}^3$ with r being the index of resolution level, and outputs of the fusion block $\{h'_r\}_{r=0}^3$ are



computed as the average of transformed features: $h'_r = \frac{1}{4} \cdot (T_{0r}(h_0) + T_{1r}(h_1) + T_{2r}(h_2) + T_{3r}(h_3))$. The transform function $T_{xr}(\cdot)$ is decided by input resolution level index x and output resolution level index r . If $x < r$, the input features are downsampled for $r - x$ rounds; If $x > r$, the input features are upsampled for $x - r$ rounds; While $T_{xr}(h) = h$ when $x = r$.

Next, we will demonstrate the downsampling and upsampling operations between two neighboring levels M^{n+1} and M^n . With the constructed bijective map $\mathcal{H}_n : M^{n+1} \rightarrow M^n$ in the previous section, we can easily adapt the pooling and unpooling operations in images to irregular mesh data and then achieve feature fusion. Our downsampling and upsampling operations utilize mesh self-parameterization as clustering tools and precisely aggregate the representation through the layer.

Downsampling. Firstly, we compute a sparse face mapping matrix $A^n = \{a_{i,j}^n\} \in \mathbb{R}^{|F^{n+1}| \times |F^n|}$, where $a_{i,j}^n$ measures the overlap ratio between the face f_j^n of M^n and the image $\mathcal{H}^n(f_i^{n+1})$ of the face f_i^{n+1} of M^{n+1} (see Figure. 7) via the following equation:

$$a_{i,j}^n = \frac{S(\mathcal{H}^n(f_i^{n+1}) \cap f_j^n)}{S(f_j^n)}. \quad (5)$$

$S(\cdot)$ computes the planar polygon area. Then we propose a weighted average fusion method to define the downsampling operation from mesh M^{n+1} to mesh M^n as follows:

$$h_{j,n}^F = \frac{\sum_i a_{i,j}^n \cdot h_{i,n+1}^F}{\sum_i a_{i,j}^n}, \quad (6)$$

where $h_{i,n+1}^F$ represents the feature vector for face f_i^{n+1} and $h_{j,n}^F$ represents the pooled feature vector for face f_j^n .

In practice, we obtain the multi-resolution meshes by sequentially applying a fixed number of edge collapse till the number

of vertices reaches the target for each resolution level. As mesh M^{n+1} with $|F^{n+1}|$ faces has been decimated to M^n with $|F^n|$ faces, the downsampling rate between two neighboring levels is defined as $|F^{n+1}|/|F^n|$. The downsampling rate is a hyper-parameter for our network; we decide it together by the number of faces of the finest mesh and base mesh, and the height of the pyramid. In our experiments, it is empirically set to 4 for training datasets.

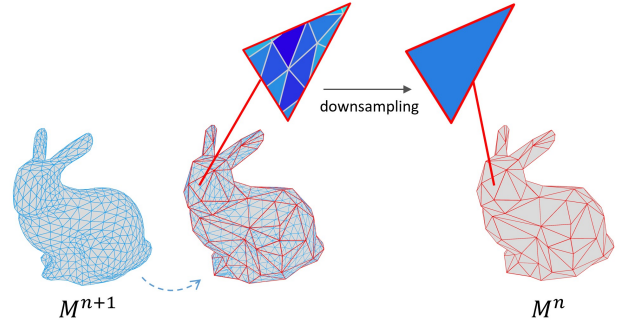


Figure 7: Visualization of the downsampling process: A cluster of faces from mesh M^{n+1} contributes to one face in the decimated mesh M^n , where the contribution score α is determined by the intersection area.

Upsampling. The upsampling operation can be seen as the reverse of downsampling. With the sparse face mapping matrix A^n , we define the area-aware upsampling operation as follows:

$$h_{i,n+1}^F = \frac{\sum_j a_{i,j}^n \cdot h_{j,n}^F}{\sum_j a_{i,j}^n}. \quad (7)$$

From the above equation, we can see that if face image $\mathcal{H}(f_i^{n+1})$ is fully contained in face f_j^n , then feature $h_{j,n}^F$ of face f_j^n is directly assigned to face f_i^{n+1} . As the sampling rate increases, more faces of mesh M^{n+1} end up sharing the same upsampled feature, resulting in the process resembling nearest neighbor sampling. Thus, the generated feature maps could be very sparse and unlikely to depict semantically consistent regions [41]. To improve this, we propose a more effective upsample operation based on barycentric interpolation. We first compute a feature $h_{i,n}^V$ for each vertex v_i^n of M^n by averaging its incident faces features $h_{j,n}^F$:

$$h_{i,n}^V = \frac{1}{N(v_i^n)} \sum_{j \in N(v_i^n)} h_{j,n}^F, \quad (8)$$

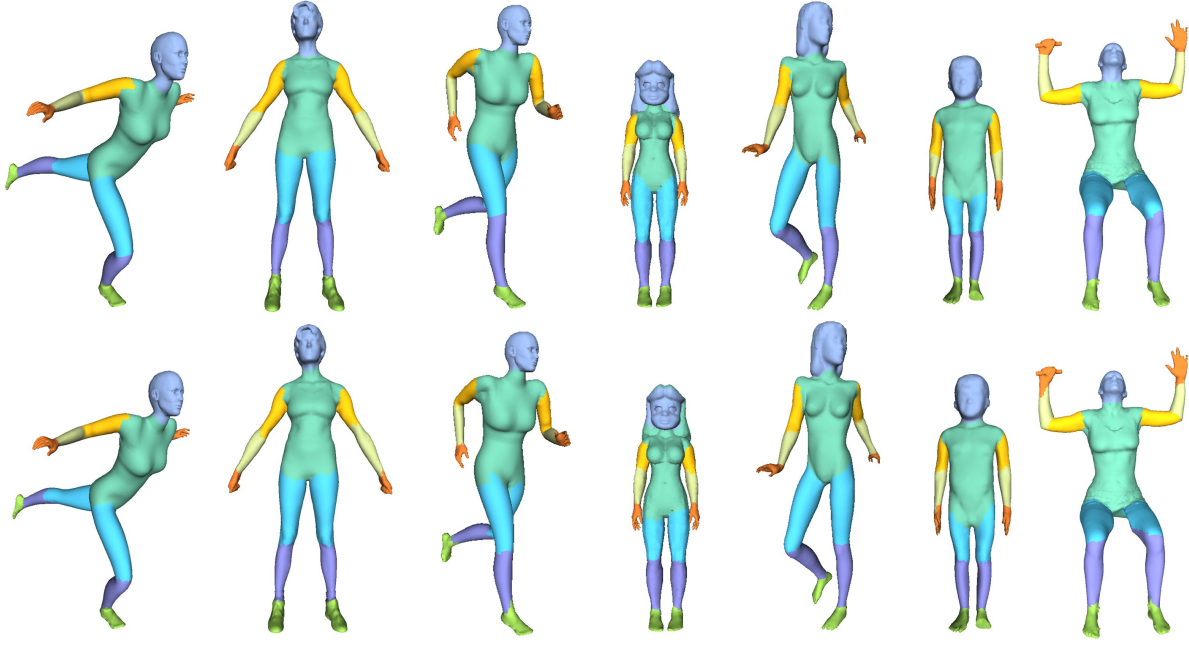


Figure 8: Visualization of segmentation results. Top: SPMM-Net segmentation results. Bottom: ground truth.

where $\mathcal{N}(v_i^n)$ is the 1-ring vertex-neighbourhood of v_i^n . Then, we interpolate the vertex feature for each vertex v_i^{n+1} of M^{n+1} via:

$$h_{i,n+1}^V = \alpha h_{i_1,n}^V + \beta h_{i_2,n}^V + (1 - \alpha - \beta) h_{i_3,n}^V. \quad (9)$$

$\{h_{i_1}^V, h_{i_2}^V, h_{i_3}^V\}$ are vertex features of the triangle where $\mathcal{H}^n(v_i^{n+1})$ lies and (α, β) are the corresponding barycentric coordinates. Lastly, we compute each face feature $h_{i,n+1}^F$ of M^{n+1} as the average of its incident vertex features:

$$h_{i,n+1}^F = \frac{1}{3} \sum_{j=1}^3 h_{i_j,n+1}^V. \quad (10)$$

5. Experiments

This section reports our experimental results and highlights the effectiveness of our proposed framework. We conducted evaluations on dense prediction for meshes, including mesh segmentation and shape correspondence. We also performed comparisons of our approach with the state-of-the-art and assessed the key components of our network. The results provide convincing evidence of the superior performance of our framework in accomplishing these tasks.

5.1. Implementation

Dataset. Since our method targeted dense prediction tasks, we required the input mesh to contain more than 10,000 faces. Additionally, the input mesh should be watertight, so we utilized hole-filling algorithms to repair meshes that contain holes or boundaries. Subsequently, we constructed a set of multi-resolution meshes and a collection of bijective surface-to-surface maps using the method described in Section 3. The weight w for linear combination the approximation error E_{approx} and the distortion error $E_{distort}$ is set to 0.1. Our experiments encompassed several datasets, including the human body segmentation

dataset [42], COSEG dataset [43], and FAUST shape correspondence dataset [44]. The meshes in the COSEG dataset are of low-resolution, and therefore, we processed meshes in the dataset and generated high-resolution data.

Augmentation. Given a high-resolution input M^K , we generated a few variations of decimated mesh pyramids to reduce the variance introduced by using different edge collapse orderings. That is, we constructed several collections of surface-to-surface maps for each input mesh. The procedure helps to reduce the influence of the decimation and improve the robustness of the model. However, as the augmentation also increases the training time and computational cost, it is necessary to balance the benefits against these considerations.

Following the process outlined in [13], we scaled each input mesh to fit into a unit cube and applied a random scaling with a normal distribution $\mu = 1$ and $\sigma = 0.1$, in order to reduce the network’s sensitivity to the size of the model. As some datasets contain meshes with different orientations, we further applied a random rotation along the $[x, y, z]$ axes with Euler angles of $[0, \pi/2, \pi, 3\pi/2]$, in accordance with the settings in [15]. These measures aimed to increase the diversity of the training data and enhance the robustness and generalization performance of the proposed model.

Networks. The proposed framework employs HRNetV2p [12] as the backbone feature extractor. In our framework, a multi-resolution block consists of a parallel convolution block and a multi-resolution fusion block. Each parallel convolution block comprises four residual units, and each residual unit is composed of two face convolution layers, two batch normalization layers, and two ReLU layers. The implemented network contains four resolution levels and four stages, with the number of feature channels for each resolution level set to $[C, 2C, 4C, 8C]$. The network starts with four bottleneck units in the first stage, followed by a downsampling operation. Consistent with the settings in HRNetV2p, the second, third, and fourth stages of the network contain one, four, and three multi-resolution blocks, respectively. The outputs from the multi-resolution levels are concatenated to generate a $15C$ -dimensional vector, which is passed through a

linear classifier or regressor to make predictions. This design leverages the strengths of the HRNet architecture and enables effective feature extraction across different resolution levels.

5.2. Segmentation tasks

We utilized the HRNetV2p-W32 architecture, with 32 indicating the number of channels of the high-resolution convolutions, and 64, 128, 256 being the number of channels for the 2nd, 3rd, and 4th resolution levels, respectively. To facilitate cross-resolution feature fusion, we employed area-weighted downsampling and barycentric upsampling techniques. For the segmentation tasks, we used the cross-entropy loss function. The SGD optimizer was used with an initial learning rate of $2e^{-2}$, momentum of 0.9, and weight decay of 0.0005. The network was trained for 200 epochs with a batch size of 4 on NVIDIA Quadro RTX 5000, for 14 hours. Our network takes high-resolution meshes containing approximately 16,384 faces per mesh as input. We constructed the mesh pyramid by sequentially reducing the number of faces to 4,096, 1,024, and 256, with a downsampling rate of 4, resulting in a mesh pyramid with a depth of 4.

Human body segmentation dataset. We evaluated our SPMM-Net on the human body segmentation dataset [42], which aims to predict the probability of each triangular face belonging to a specific part of the mesh. The dataset consists of 381 training human models and 18 testing models from various datasets, with each model segmented into 8 labels. Different from SubdivNet [15], we didn’t generate multiple instances of each input mesh, as our method directly deals with irregular input data and provides more stable and robust results.

To ensure a fair comparison with other methods, we presented the segmentation results on the original resolution human body segmentation dataset. From Table. 1, we achieved comparable segmentation results with other state-of-the-art methods. Some segmentation results are visualized in Figure. 8. It’s worth noting that the highest accuracy reported in SubdivNet [15] used the majority voting strategy, which involves remeshing the test data 10 times and using the predictions from different remeshed shapes to make the final prediction. However, the strategy increases the training time and computation cost by $\times 10$ time.

Table 1: Segmentation accuracy on human body segmentation dataset [42].

Method	Accuracy
PointNet++ [45]	82.3%
PD-MeshNet [14]	86.9%
DiffusionNet [46]	91.7%
SubdivNet [15]	91.1%
SPMM-Net	91.9%

Figure 9 displays a qualitative comparison between the segmentation results obtained by MeshCNN [13] and SPMMNet. Despite taking input meshes of different resolutions, both methods performed three pooling operations on the input meshes to obtain a base mesh consisting of approximately 300 to 400 faces. We observe that our method better preserves the human shape and results in higher segmentation accuracy. Notably, the shoulders of the model underwent significant changes in the base mesh generated by MeshCNN’s pooling method, leading to a drop in segmentation accuracy in this region.

COSEG dataset. We also evaluated our SPMM-Net on the COSEG dataset [43]. The dataset contains three large sets of meshes, including 200 alien models, 300 vase models, and 400

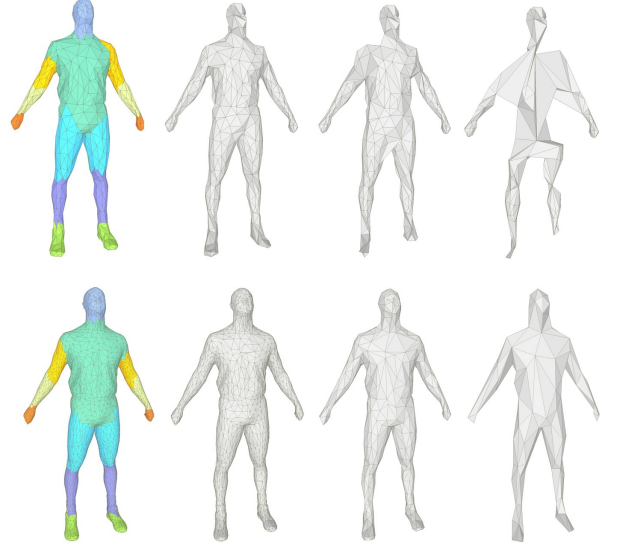


Figure 9: Segmentation results on the Human body dataset using MeshCNN [13] (Top left) and SPMMNet (Bottom left). The results of intermediate pooling operations are shown in sequence. We observe smaller distortions of the pooled meshes with our method.

chair models. As original COSEG datasets contain non-manifold meshes, we fixed the meshes and generated corresponding high-resolution data. The training was conducted on three datasets independently. We used the soft boundary labels [14] to measure the prediction of each face that is incident to the boundary. Quantitative results are shown in Table. 2. It can be seen that our method performs the best in all categories. We believe that this is due to the uniform propagation scheme through multi-resolution levels. To further show this, we visualize the decimated mesh sequences of the test data in Figure. 10.

Table 2: Segmentation accuracy on COSEG dataset [43].

Method	Vase	Chair	Alien
MeshCNN [13]	85.2%	92.8%	94.4%
PD-MeshNet [14]	81.6%	90.0%	89.0%
SubdivNet [15]	96.7%	96.7%	97.3%
SPMM-Net	97.0%	97.2%	97.6%

Moreover, due to the loop connectivity requirement in SubdivNet, creating a mesh pyramid that precisely describes the original shape is a demanding task. However, as shown in Figure. 11, our method is flexible to connectivity. Therefore, we can generate a mesh pyramid with higher quality that enhances the learning process.

5.3. Shape correspondence tasks

We validated our method on Faust [44] shape correspondence and compared the results with approaches to [20][21][47] that employ the Princeton benchmark protocol[48]. The shape correspondence task in these works refers to the task of labeling each vertex of the input shape to the corresponding vertex of the reference shape. The Faust dataset contains 100 processed scanned human body shapes with ten different poses. Each shape has 6890 nodes and 13776 faces. The first 80 shapes from the dataset are used for training and the rest 20 shapes for testing. The ground truth of the dataset is given implicitly, as each shape

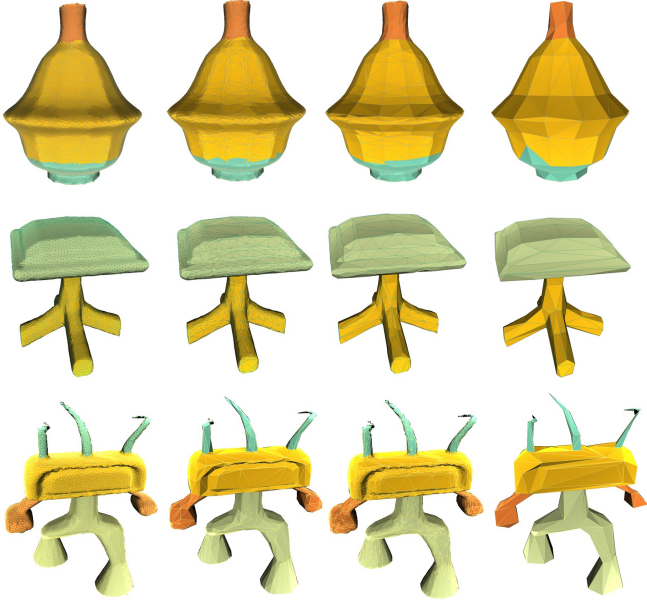


Figure 10: Segmentation results on COSEG dataset [43]. The segmentation prediction of high-resolution input is shown on the left, followed by the decimated meshes after each downsampling operation. For visualization purpose, we propagated the prediction on high-resolution mesh to intermediate levels.

has the same connectivity. We took the original meshes as input and constructed the mesh pyramids with number of faces equals to 3444, 861, and 216, with downsampling rate equals to 4.

As our SPMM-Net deals with the face element, we formulated the correspondence problem as a face labeling task, where each face was assigned a 13776-dimensional vector as ground truth. We employed the HRNetV2p-W48 architecture for this pretty dense task, meaning the resolution level 1st, 2nd, 3rd, and 4th contains 48, 96, 192, 384 convolution channels, respectively. We used the area-weighted downsampling and barycentric upsampling for feature fusion, and employed a soft error loss [49]. For each input mesh, we first calculated the geodesic distance between the centers of any pair of triangle faces, then, for predictions that are geodesically far away from the correct face, we punished them stronger. We used the same SGD optimizer with segmentation tasks. The SGD optimizer was used with an initial learning rate of $2e^{-2}$, momentum of 0.9, and weight decay of 0.0005. The network was trained for 200 epochs with a batch size of 4 on NVIDIA Quadro RTX 5000, for 8 hours.

The correspondence error is calculated as the normalized geodesic distance between the predicted face center and the ground truth face center. To measure the correspondence quality, the Princeton benchmark protocol counts the percentage of derived correspondence within a geodesic radius r around the correct face center. Our method achieves state-of-the-art results compared with the methods using the same protocol (See Table.3). The derived errors are visualized in Figure. 12, and we can see that the second to the right body presents a higher geodesic error as the posture is rarely seen in the dataset.

5.4. Further Evaluation

We conducted further evaluations to assess the effectiveness of the key components in the proposed method on the human body segmentation dataset. The first experiment focused on evaluating the impact of image dense prediction architectures on 3D mesh learning. To this end, we implemented and compared two popu-

Table 3: Correspondence accuracy on FAUST dataset[44].

Method	Accuracy (r=0)	Accuracy (r=0.01)
MoNet [20]	88.20%	92.35%
SplineCNN [21]	99.12%	99.37%
ACSCNN [47]	98.98%	99.64%
SPMM-Net	99.37%	99.68%

lar architectures for image segmentation, namely U-Net and HRNetv2. Our results indicate that HRNetv2 outperforms U-Net in 3D mesh learning, similar to the image tasks.

Meanwhile, to evaluate the effectiveness of proposed weighted-average downsample and upsample operations, we tested two architectures with the method proposed in SubdivNet [15]. We built 4-level mesh sequences with loop connectivity using the method mentioned in the paper, resulting in the same resolution data (16384 faces) as input. We adopted identical network settings and training, while the only differences were the downsampling and upsampling operations. The results show that our method achieves better performance in mesh dense predictions.

Table 4: Ablation study on network architectures evaluated on human body segmentation dataset [42].

Method	Architecture	Accuracy
SubdivNet [15]	U-Net [6]	89.5%
SPMM-Net	U-Net [6]	90.2%
SubdivNet [15]	HRNet [12]	90.8%
SPMM-Net	HRNet [12]	91.9%

Table. 5 compares segmentation networks trained with different input face numbers and downsampling rates. The results show that deeper networks yield higher segmentation accuracy with the same input face number and base face number. We also demonstrate that we can achieve the same base size with different input mesh sizes by adjusting the downsampling rate. No significant difference was observed between the different input sizes.

Table 5: Ablation study on decimation algorithm and downsample rate on human body segmentation dataset [42].

#Input faces	rate	#Paramids faces	Accuracy
16384	4	[16384, 4096, 1024, 256]	91.9%
16384	8	[16384, 2048, 256]	91.1%
9216	6	[9216, 1536, 256]	91.5%

6. Conclusions

We have presented SPMM-Net, a novel deep learning framework designed for 3D meshes to address dense prediction tasks. Behind SPMM-Net are the construction of a multi-resolution mesh pyramid, incorporating sequential bijective mapping relationships, the design of flexible and robust downsampling/upsampling and convolution operations for irregular high-resolution meshes, and the design of the multi-resolution network that maintains high-resolution representations throughout

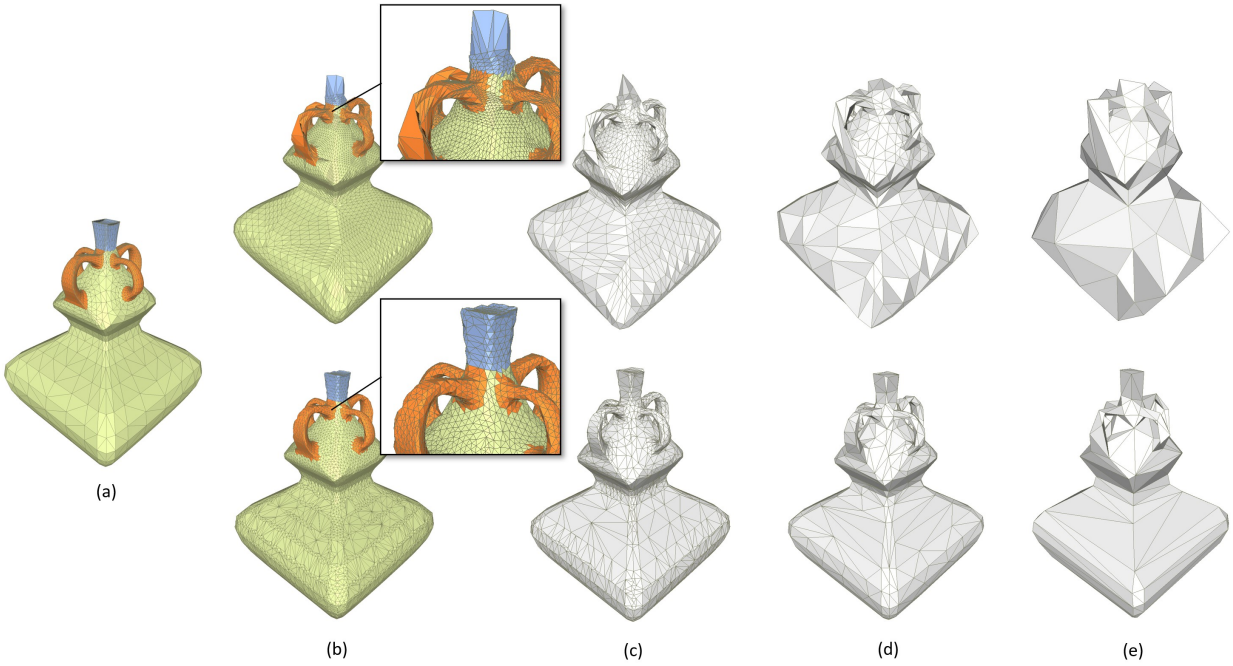


Figure 11: The mesh pyramids constructed by SubdivNet [15] (first row) and SPMM-Net (bottom row). (a) Low-resolution ground truth. (b) High-resolution inputs to the network with 16384 faces. (c)-(e) Decimated meshes contain 4096, 1024, and 256 faces, respectively. SubdivNet decimates the original mesh to base size (256 faces) first and then subdivides the base mesh to create loop connectivity, while our method remeshes the input first and decimates the high-resolution mesh level by level to better preserve the original shape.

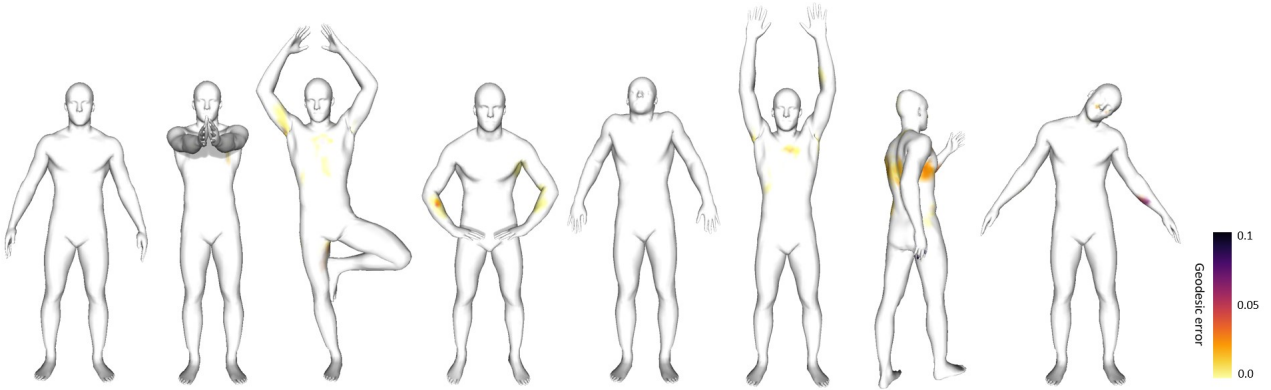


Figure 12: Shape correspondence for FAUST dataset [44].

the network. The key feature of our approach is the bijective inter-surface mapping that redefines meshes, rather than simply reshaping them. Extensive experiments have demonstrated that the proposed framework can effortlessly adapt to existing CNN architectures and learn robust face features for dense prediction tasks.

Though our network exhibits flexibility with respect to the connectivity of the input mesh, we require the mesh to be manifold so that the self-parameterization algorithm can be applied. Also, it should be pointed out that the quality of input meshes and the choice of self-parameterization methods impact the pooling and unpooling results. Another limitation of our method is that it does not support some CNN operations such as strided convolution and dilated convolution. We hope to extend our work to overcome these issues in future.

References

- [1] A. Krizhevsky, I. Sutskever, G. E. Hinton, Imagenet classification with deep convolutional neural networks, in: Proceedings of the 25th International Conference on Neural Information Processing Systems - Volume 1, NIPS'12, 2012, p. 1097–1105.
- [2] K. Simonyan, A. Zisserman, Very deep convolutional networks for large-scale image recognition, in: International Conference on Learning Representations, 2015.
- [3] K. He, X. Zhang, S. Ren, J. Sun, Deep residual learning for image recognition, 2016 IEEE Conference on Computer Vision and Pattern Recognition (CVPR) (2016) 770–778.
- [4] H. Noh, S. Hong, B. Han, Learning deconvolution network for semantic segmentation, in: Proceedings of the IEEE international conference on computer vision, 2015, pp. 1520–1528.
- [5] V. Badrinarayanan, A. Kendall, R. Cipolla, Segnet: A deep convolutional encoder-decoder architecture for image segmentation, IEEE Transactions on Pattern Analysis and Machine Intelligence 39 (12) (2017) 2481–2495.
- [6] O. Ronneberger, P. Fischer, T. Brox, U-Net: Convolutional networks for biomedical image segmentation, Medical Image Computing and Computer-Assisted Intervention – MICCAI 2015.

- [7] A. Newell, K. Yang, J. Deng, Stacked hourglass networks for human pose estimation, in: *Computer Vision – ECCV 2016*, Springer International Publishing, 2016, pp. 483–499.
- [8] H. Zhao, J. Shi, X. Qi, X. Wang, J. Jia, Pyramid scene parsing network (2017) 6230–6239.
- [9] L.-C. Chen, G. Papandreou, I. Kokkinos, K. Murphy, A. L. Yuille, Deeplab: Semantic image segmentation with deep convolutional nets, atrous convolution, and fully connected crfs, *IEEE Transactions on Pattern Analysis and Machine Intelligence* 40 (4) (2018) 834–848.
- [10] L.-C. Chen, Y. Zhu, G. Papandreou, F. Schroff, H. Adam, Encoder-decoder with atrous separable convolution for semantic image segmentation, in: *ECCV*, 2018.
- [11] K. Sun, B. Xiao, D. Liu, J. Wang, Deep high-resolution representation learning for human pose estimation, in: *Proceedings of the IEEE Conference on Computer Vision and Pattern Recognition (CVPR)*, 2019.
- [12] J. Wang, K. Sun, T. Cheng, B. Jiang, C. Deng, Y. Zhao, D. Liu, Y. Mu, M. Tan, X. Wang, W. Liu, B. Xiao, Deep high-resolution representation learning for visual recognition, *Proceedings of IEEE Transactions on Pattern Analysis and Machine Intelligence (TPAMI)*.
- [13] R. Hanocka, A. Hertz, N. Fish, R. Giryes, S. Fleishman, D. Cohen-Or, Meshcnn: a network with an edge, *ACM TOG* (2019) 90.
- [14] F. Milano, A. Loquercio, A. Rosinol, D. Scaramuzza, L. Carlone, Primal-dual mesh convolutional neural networks, in: *Conference on Neural Information Processing Systems (NeurIPS)*, 2020.
- [15] S.-M. Hu, Z.-N. Liu, M.-H. Guo, J.-X. Cai, J. Huang, T.-J. Mu, R. R. Martin, Subdivision-based mesh convolution networks, *ACM Trans. Graph.* 41 (3) (2022) 25:1–25:16.
- [16] M. Garland, P. S. Heckbert, Surface simplification using quadric error metrics, in: *Proceedings of the 24th Annual Conference on Computer Graphics and Interactive Techniques, SIGGRAPH '97*, ACM Press/Addison-Wesley Publishing Co., USA, 1997, p. 209–216.
- [17] J. Schreiner, A. Asirvatham, E. Praun, H. Hoppe, Inter-surface mapping, *ACM TOG* 23 (3) (2004) 870–877.
- [18] A. Khodakovsky, N. Litke, P. Schröder, Globally smooth parameterizations with low distortion, *ACM TOG* 22 (3) (2003) 350–357.
- [19] J. Masci, D. Boscaini, M. M. Bronstein, P. Vandergheynst, Geodesic convolutional neural networks on riemannian manifolds, *IEEE International Conference on Computer Vision Workshop (ICCV)* (2015) 832–840.
- [20] F. Monti, D. Boscaini, J. Masci, E. Rodolà, J. Svoboda, M. M. Bronstein, Geometric deep learning on graphs and manifolds using mixture model cnns, *Proceedings IEEE Conference on Computer Vision and Pattern Recognition (CVPR)* (2017) 5425–5434.
- [21] M. Fey, J. Lenssen, F. Weichert, H. Muulle, Splinecnn: Fast geometric deep learning with continuous b-spline kernels, *Proceedings of the IEEE Conference on Computer Vision and Pattern Recognition (CVPR)* (2018) 869877.
- [22] Y. Feng, Y. Feng, H. You, X. Zhao, Y. Gao, Meshnet: Mesh neural network for 3d shape representation, in: *Proceedings of the AAAI Conference on Artificial Intelligence*, Vol. 33, 2019, pp. 8279–8286.
- [23] J. Schult, F. Engelmann, T. KonACM TOGianni, B. Leibe, Dualconvmeshnet: Joint geodesic and euclidean convolutions on 3d meshes, 2020, pp. 8609–8619.
- [24] X.-J. Li, F.-L. Yang, Jieand Zhang, Laplacian mesh transformer: Dual attention and topology aware network for 3d mesh classification and segmentation, in: *Computer Vision – ECCV 2022*, 2022, pp. 541–560.
- [25] A. Lahav, A. Tal, Meshwalker: Deep mesh understanding by random walks, *ACM TOG* 39 (6) (2020) 1–13.
- [26] M. Defferrard, X. Bresson, P. Vandergheynst, Convolutional neural networks on graphs with fast localized spectral filtering, *Advances in Neural Information Processing Systems (NIPS)* (2016) 3837–3845.
- [27] Z. Ying, J. You, C. Morris, X. Ren, W. Hamilton, Jure, Hierarchical graph representation learning with differentiable pooling, *Advances in Neural Information Processing Systems (NIPS)* (2018) 4800–4810.
- [28] H.-T. D. Liu, V. G. Kim, S. Chaudhuri, N. Aigerman, A. Jacobson, Neural subdivision, *ACM Trans. Graph.* 39 (4).
- [29] N. Aigerman, R. Poranne, Y. Lipman, Lifted bijections for low distortion surface mappings, *ACM TOG* 33 (4) (2014) 1–12.
- [30] P. Schmidt, J. Born, M. Campen, L. Kobbelt, Distortion-minimizing injective maps between surfaces, *ACM TOG* 38 (6).
- [31] N. Aigerman, Y. Lipman, Orbifold tutte embeddings., *ACM TOG* 34 (6) (2015) 190–1.
- [32] N. Aigerman, S. Z. Kovalsky, Y. Lipman, Spherical orbifold tutte embeddings, *ACM TOG* 36 (4).
- [33] P. Schmidt, M. Campen, J. Born, L. Kobbelt, Inter-surface maps via constant-curvature metrics, *ACM TOG* 39 (4).
- [34] V. Kraevoy, A. Sheffer, Cross-parameterization and compatible remeshing of 3d models, *ACM TOG* 23 (3) (2004) 861–869.
- [35] H.-T. Liu, J. Zhang, M. Ben-Chen, A. Jacobson, Surface multigrid via intrinsic prolongation, *ACM Transactions on Graphics* 40 (2021) 1–13.
- [36] B. Lévy, S. Petitjean, N. Ray, J. Maillot, Least squares conformal maps for automatic texture atlas generation, *ACM TOG* 21 (3) (2002) 362–371.
- [37] A. W. F. Lee, W. Sweldens, P. Schröder, L. Cowsar, D. Dobkin, MAPS: Multiresolution adaptive parameterization of surfaces, in: *Proceedings of SIGGRAPH 98*, 1998, pp. 95–104.
- [38] P. J. Brown, C. T. Faigle, A robust efficient algorithm for point location in triangulations, *Tech. rep.*, University of Cambridge, Computer Laboratory (1997).
- [39] C. Mccoid, M. J. Gander, A provably robust algorithm for triangle-triangle intersections in floating-point arithmetic, *ACM Trans. Math. Softw.* 48 (2).
- [40] A. Hertz, R. Hanocka, R. Giryes, D. Cohen-Or, Deep geometric texture synthesis, *ACM TOG* 39 (4).
- [41] H. Lu, Y. Dai, C. Shen, S. Xu, Indices matter: Learning to index for deep image matting, in: *Proceedings of the IEEE/CVF International Conference on Computer Vision (ICCV)*, 2019.
- [42] H. Maron, M. Galun, N. Aigerman, M. Trope, N. Dym, E. Yumer, V. G. Kim, Y. Lipman, Convolutional neural networks on surfaces via seamless toric covers, *ACM TOG*.
- [43] Y. Wang, S. Asafi, O. van Kaick, H. Zhang, D. Cohen-Or, B. Chen, Active co-analysis of a set of shapes 31 (6).
- [44] F. Bogo, J. Romero, M. Loper, M. J. Black, Faust: Dataset and evaluation for 3d mesh registration, *Proceedings of the IEEE Conference on Computer Vision and Pattern Recognition (CVPR)* (2014) 3794–3801.
- [45] C. R. Qi, L. Yi, H. Su, L. J. Guibas, Pointnet++: Deep hierarchical feature learning on point sets in a metric space, in: *Proceedings of the 31st International Conference on Neural Information Processing Systems*, 2017, p. 5105–5114.
- [46] N. Sharp, S. Attai, K. Crane, M. Ovsjanikov, Diffusionnet: Discretization agnostic learning on surfaces 41 (3).
- [47] Q. Li, S. Liu, L. Hu, X. Liu, Shape correspondence using anisotropic chebyshev spectral cnns, in: *2020 IEEE/CVF Conference on Computer Vision and Pattern Recognition (CVPR)*, 2020, pp. 14646–14655.
- [48] V. G. Kim, Y. Lipman, T. Funkhouser, Blended intrinsic maps, *ACM TOG* 30 (4).
- [49] O. Litany, T. Remez, E. Rodolà, A. M. Bronstein, M. M. Bronstein, Deep functional maps: Structured prediction for dense shape correspondence, *2017 IEEE International Conference on Computer Vision (ICCV)* (2017) 5660–5668.